# USE OF COMPUTED TOMOGRAPHY FOR CHARACTERIZING MATERIALS GROWN TERRESTRIALLY AND IN MICROGRAVITY

## Donald C. Gillies[1*] and H. Peter Engel[2]

MSFC/NASA[1] and Wyle Labs/JSC/NASA[2]

Computed Tomography (CT) has advanced considerably since being responsible for such dramatic advances in diagnostics within the medical field.[1] It has become a major tool in non destructive evaluation (NDE), and is used in many fields as diverse as coal-mining[2] to metal solidification[3] to examination of rock cores.[4] A review of industrial applications has been written by Dennis.[5] It is only recently that the technique has been seriously used to determine composition through precise measurement of density.[6] While such applications are restricted to cases when there is no ambiguity in the relationship of composition to density. Thus alloy solid solutions lend themselves to compositional analysis provided there is a large change in density with composition. The technique is most useful when rapid non-destructive evaluation is needed. Such cases will occur with samples returning from the International Space Station (ISS) when knowledge of the results could affect future strategies for processing of on-board samples. Experiments from those Principal Investigators (PI) that are most likely to benefit from early CT scanning are discussed. With a dearth of samples, the major emphasis in the first part of this project has been on preparing suitable standards, optimizing the CT technique for these applications, and using the CT system to determine density variations with temperature. An interesting application of CT has been in the examination of meteorites, which can be classified as space-grown materials and will certainly have solidified in a low gravity environment.

**Theoretical Background to CT**

The theory behind CT and particularly high energy CT (X-Ray) has been well described in the literature and will only be described briefly here. Fundamentally, a tomography system operates by measuring the intensity of a linear beam after attenuation by a volumetric sample. The sample (or samples) is moved and the attenuations collected from multitudinous directions. Mathematically, Radon[7] discovered a method of transforming the many intensity readings into individual 2-dimensional absorption values. In specific cases these absorption values can be correlated directly to composition.

For adequate penetration of engineering samples, high energy beams such as X-Rays or gamma rays are necessary. The interaction of such beams with matter is shown schematically in Figure 1. Of specific interest is that within the Compton scattering regime, the absorption coefficient is directly proportional to the atomic number of the scattering center. This is not the case with the low energy region (dominated by photoelectric absorption), and in the high energy region (mainly pair production). The dominant interaction regions are shown as functions of mass attenuation coefficient ($cm^2$/g)and atomic number with respect to photon energy are shown in Figure 2. Superimposed on this diagram is the energy of the $^{60}$Co radioisotope which is the primary beam used in this work. $^{60}$Co produces two energy levels of gamma rays, at 1.17 and 1.30 Mev. Of specific interest is that the absorption levels of these two energies is low enough that we can consider the system to be monochromatic.

* Corresponding author. e-mail: donald.gillies@msfc.nasa.gov

Effectively, each incident beam of initial intensity $I_0$, passing through the system is attenuated to the transmitted value I, with the attenuation being a function of the linear attenuation coefficient μ, and the thickness, s.

Effectively $$I = I_0 \exp(-\mu s) \qquad (1)$$

Along the entire path length, the attenuation is additive so that

$$I = I_0 \exp-(\mu_1 s_1 + \mu_2 s_2 + \ldots + \mu_n s_n), \qquad (2)$$

where $\mu_n$ is the linear absorption coefficient of the nth element in the path and $s_n$ is its thickness.
In two dimensions and in terms of the active CT system, the position of the nth element can be described by coordinates x and y, so that the attenuation is

$$I = I_0 \exp[-\int_{source}^{detector} (x,y)ds] \qquad (3)$$

This equation becomes the Radon transformation of μ(x,y), the fundamental equation of the CT process

$$P = \ln (I_0/I) = \int_{source}^{detector} (x,y)ds \qquad (4)$$

The Radon transformation is shown in Figure 3. Basically these equations can be solved analytically from an infinite set of these integrals.

**Practical Aspects of CT for Density Measurement**
Effectively, the CT instrument measures a CT number for each x,y coordinate within a slice of a sample. Gray scale images can be obtained from the CT number to represent the absorption of the sample. This procedure is shown for a series of elemental standard materials of different, but known densities. Results produced by the ^{60}Co source as compared to an x-ray generator are shown in Figure 4. The darker the spot, the denser is the sample. The elements range in density from silicon and aluminum to lead and mercury. Some of the samples are porous, while others clearly show that an encasing fused silica tube is present. This figure also illustrates why the radioisotope is preferred for precise analytical work. The streaking evident in the x-ray image is the result of the continuous spectrum or Bremsstrahlung nature of the energy. The low energy x-rays are preferentially absorbed at the surfaces of samples so that the incident flux at the centers of the samples has a different energy spectrum from the edges. In this photograph, the streaks reflect that. In a quantitative analysis, the center would seem to be absorbing less than the surface, and an incorrect interpretation of absorption would result. The ^{60}Co source is effectively monoenergetic and avoids this problem.

The measurement of the CT number is also critical, as different values can be obtained by using different procedures. A distribution of CT numbers occurs across an entire two-dimensional section. Each absorbing element would have its own specific CT number so that a histogram is produced. In practice the sampling is limited to the region of interest which may include an encasing fused silica tube. Such a technique is shown in Figure 5. The histogram includes peaks for air, fused silica and copper. Selection of the appropriate CT number has been the subject of much investigation, particularly as the curve may not be centro-symmetric. Mode, peak position and several other mathematical functions have been tried, but the most important criterion is to use the same function for standards as for the sample being investigated.

The next step is to take the CT numbers for each sample and plot them against the density. The use of electron density (electrons per cubic Angstrom) can also be used for crystalline solids. Generally the calibration line thus produced has $R^2$ of 99%. A typical example is shown in Figure 6. While many of the standards are specifically made for the CT, in some cases problems arise because of porosity, which effectively reduces the density. In practice it was found that the use of end members as standards was the best solution for binary alloy systems.

**Early Examples**

The technique was first applied to determining compositional variations along ingots of mercury-cadmium telluride, a solid solution of cadmium telluride and mercury telluride, having a large density difference between the two end members. Macrocomposition values along a directionally solidified ingot are essential for determining the growth mechanism and the relative contributions of density driven convection and diffusion. In the past this has been done by the destructive and tedious technique of cutting and weighing the samples in air and in boiled (de-aerated) water. The CT technique proved superior without any loss of resolution. In figure 7, a sample grown at 0.1 μm/s is shown. This was to be the precursor for a sample to be flown on the fourth United States Microgravity Payload (USMP-4) flight mission, and required that the material be fabricated from several starting boules to obtain the initial desired composition profile. As cutting the sample into 2 mm slices to determine composition was undesirable, the CT method was applied to determine how best to fabricate the flight samples. Figures 8 and 9 respectively show the composition variation on the ground truth and flight samples, and also how the readings compare with electron microprobe analysis (wavelength dispersive) of the surfaces. There are definite differences in the readings. First of all, the CT will average the composition through a slice whereas the wavelength dispersive technique measures only the surface value. In the flight sample, problems with the translation device led to periodic fluctuations in the composition during the slow growth region (below 40 mm) which can be seen only with the microprobe. The quenched region (beyond 40 mm) also shows large fluctuations in the surface regions. Average readings as from the CT are essential for interpreting the growth process.

**Candidates for CT Measurement from the Flight Program**

As described above, the main requirement for composition determination via CT and density are that there be a measurable density difference between the constituent members. While originally intended for examining solid solutions such as mercury cadmium telluride, macrosegregation in directionally solidified eutectics and monotectics could also be revealed. The limitation is the spatial sensitivity of the technique. Candidates from the flight program are shown in Table 1. Fripp[8], Lehoczky[9] and Szofran[10] are using solid solution materials, while Poirier[11] and Trivedi[12] will grow eutectic material with two phases. The table shows the densities and density differences between end members. For the eutectics, the presumed eutectic composition density and the end member (assuming a divorced eutectic structure) are given. While not in this table, the flight program of German (liquid phase sintering)[13], Andrews (monotectic materials)[14], and Stefanescu (particle behavior in composites)[15] can also benefit from CT scanning. In past microgravity campaigns, both Andrews and Stefanescu used CT scanning for examination of their Sample Ampoule Cartridge Assemblies (SACA). Thermal expansion of the melt and the behavior of containing springs for the avoiding of bubbles were critical observations.

Ground-based results for germanium-silicon alloys are shown in Figures 10 and 11. Figure 10 shows a boule solidified after an alloy ingot of Ge-Si ingot was melted back onto a germanium seed, and then

directionally solidified. The build up of silicon during the initial transient can clearly be seen. In Figure 11 is shown a prospective single crystal to be used for growth initiation of an alloy crystal. While the photograph is a digital radiograph, and shows the presence of the germanium standard, the values quoted for the density are derived from CT scans at different locations within the seed crystal. Surface microprobe work could also obtain such readings, but an advantage of the CT is that an average value is obtained so that effects of radial segregation do not influence the results.

**Density Measurements**
CT has the advantage of being able to penetrate equipment in order to examine samples. Thus it is possible to measure the density of a sample within a furnace and hence determine density as a function of temperature. This can be done during and after the melting and back through a solidification cycle. The technique has the advantage of safety in that no exposed measurements need be made, and this also improves the overall thermal homogeneity of the system. Several elements have been examined at different temperatures using the CT system. Preliminary work was done on gallium and indium, but the main thrust has been on lead and a lead-antimony alloy.

A small single zone incorporating a heat pipe has been built specifically to be incorporated on the CT system. The furnace installed on the CT system is shown in Figure 12. The CT system at Kennedy Space Center (KSC) is referred to as second generation and the CT table translates through the incident beam, rotates a few degrees and repeats several times to acquire the desired number of views. While this operation disturbs the liquid, the effect, if anything, may be advantageous in reducing temperature gradients in molten samples. This would be not be the ideal technique for examining liquid-solid interfaces during melting or solidification. The density can be measured by three different techniques. First, the length of the sample can be measured by making digital radiographs through the furnace. Secondly, the diameter of the sample can be measured while in the solid state, assuming the material has not melted against the container wall. Finally, the density of the material can be measured from the CT number, and converted to density. CT sections through the furnace and through standards are shown in Figure 13. Note that the furnace elements, the insulation, the heat pipe inner and outer walls and the heat pipe inner components all show up in addition to the lead sample and the standards. In other views, furnace thermocouples show up.

Digital radiographs of pure lead at increasing temperatures are shown in Figure 14. A plot of dilation with temperature derived from these data is shown in Figure 15. The data are influenced in the solid state by the presence of bubbles on the surface, and in the liquid state by the difficulty in reading the length as influenced by the meniscus. Nevertheless, the data are of credible quality. Figure 16 shows the density variation with temperature as measured by CT scans. The data are of excellent quality and compare with values in the literature, as can be seen from the accompanying data points.[16] At present a sample of Pb-5.8% Sb is being evaluated and has been heated to 900°C, and is being measured by CT during the cooling. Further samples have been prepared including CdTe, and several compositions of HgCdTe. These latter have proved to be problematic at high temperatures due to the need to encapsulate them safely. The CT technique enables them to be evaluated safely and enclosed satisfactorily during the measurements.

**CT of Metallic Meteorites**
In the absence of man-generated long duration microgravity samples, two meteorites have been examined by CT to determine the inner structure. The objectives are to probe for compositional differences, particularly second phases, including compositional variations and, in coarse samples, any grain size

240

differences which could aid in the determination of age or cooling rate of the structure. Such an evaluation would normally be non-destructive. Such samples are normally unique and the maximum information has to be gathered without resorting to cutting and polishing. CT is proving to be useful.

The first sample was a privately owned sample of a meteorite which was found in China in the Nantan region. The sample was considerably corroded and was used as a test case to evaluate how well CT could demonstrate the inner structure. Following CT scanning of the entire piece, which was roughly 8 cm long and 4 cm diameter, a small section was cut from the center, polished, etched and examined by electron microprobe analysis. The oxidation proved to be considerable, and penetrated well into the sample. This is shown in Figure 17b, an oxygen map of the polished surface. Figure 17a is the CT scan through the same level and clearly shows the density difference evident between the iron-nickel alloy and the iron oxide. Clearly, the resolution of CT is inferior to the microprobe work, but with coarse grained samples, much information can nevertheless be obtained.

The second meteorite examined was from the Mundrabilla region of Australia. Discovered in 1916, two large slabs of 6 and 15 tons constitute the main mass. The smaller mass is shown in Figure 18a. The 6 ton slab has been cut into several 2 inch thick slices, which are on display in several museums throughout the world. The National Museum of Natural History (NMNH) in Washington houses one polished slice over 4 foot long and 2 foot across at its widest point. The structure displayed is very unusual in that it consists of primary iron-nickel grains with iron sulfide secondary phase in between them. The sample is extremely coarse, with the primary phase several cm across, and the sulfide phase, which constitutes some 25% by volume making up channels which are often broader than 1 cm. A slab was made available by NMNH which is 80 cm x 13cm x 15cm (Figure 18b). This is thicker than any of the slices, and proved to be within the limit of the $^{60}$Co CT system. Small pieces were also made available for polishing. A typical microstructure is shown in Figure 19. The metallic phase is made up of the two common forms of the iron-nickel system found in meteorites, namely the high nickel face-centred cubic phase (taenite), and the low nickel body-centred cubic phase (kamacite). While not obvious in this sample the platelike the structure of the kamacite phase (bottom right) has been produced by a eutectoid reaction and etching has revealed the famous Widmanstätten structure. The secondary sulfide is primarily troilite (FeS), but with thin parallel plates of daubreelite ($FeCr_2S_4$) present. Many other phases were present including a conical graphite phase, an example of which is "boxed" in Figure 18b.

Initially, 15 cm of the total length has been imaged at 1 mm intervals. The location of these scans is shown in the digital radiograph of Figure 20. Note that the sample is not removed from its containing wooden crate; the handles are clearly visible. Thirty five of the CT sections are shown in Figure 21, while a typical sample is shown in Figure 22. The density difference between the sulfide and the metal phase is clear. The graphite phase referred to above has a density between the metal and the sulfide. This is higher than anticipated due to the low spatial resolution and probable eutectoid-type mixing of the graphite and the metal. These 150 sections have been sequenced into an animation, and are being prepared for 3-D visualization. While many of the microscopically visible features are not seen in the CT scans, the animation demonstrates the nature of the distribution of the sulfide with respect to the metal, the exact conical nature of the graphite and the presence of other low density rounded features within the metal. These have not yet been identified. The entire length of the sample will be finally examined.

## Conclusions

The CT technique has demonstrated the ability to perform high quality chemical composition analysis on solid solutions, and the potential for evaluating flight samples within their ampoules has also proved possible. It has been shown that in situ measurements of dilation and density are possible using a furnace installed on the CT system. Finally, the CT technique has been useful for evaluating the internal structures of two component meteorites.

## Acknowledgements

## References

1. "Computerized transverse axial scanning (tomography):Part 1. Description of system," Hounsfield G. N., *British Journal of Radiology*, 46, 1016-1022, 1973.
2. "Development of an On-line Coal Washability Analysis System Using X-Ray Computed Tomography," Lin, C. L., J. D. Miller, G. H. Luttrell and G.T. Adel, *Coal Preparation*, 21, 383-409, 2000.
3. "High-Energy X-Ray Computed Tomography of the Progression of the Solidification Front in Pure Aluminum," Hytros, Mark M., Imad M. Jureidini, Jung-Hoon Chun, Richard C. Lanza and Lannaji Saka, *Metallurgical and Materials Trans.*, 30A, 1403-1409, 1999.
4. "X-Ray Computerized Tomography," Wellington S. L. and H. J. Vinegar, *J. Petroleum Technology*, 885-898, August 1987.
5. "Industrial Computed Tomography," Dennis, Michael J., *ASM Handbook, Non Destructive Evaluation and Quality Control*, 17, 358-386, 1994.
6. "Über die Bestimmung von Funktionen durch ihre Integralwerte längs gewisser Mannigfaltigkeiten." Radon, J., *Berichte übe rdii Verhandlungen*, 69, 262-277, 1917.
7. "Quantitative Computer Tomography for Determining Composition of Microgravity and Ground Based Solid Solutions," Gillies, Donald C. and H. Peter Engel, 11th International Symposium for Experimental Methods for Microgravity Materials Research, 1999
8. "Growth of Compound Semiconductors in a Low Gravity Environment: Microgravity Growth of PbSnTe," Fripp, A. L., W. J. Debnam, W. R. Rosch, N. R. Baker and R. Narayanan Proceedings of the Microgravity Materials Science Conference, 229-234, 1998
9. "Effect of residual acceleration during microgravity directional solidification of mercury cadmium telluride on the USMP-2 mission," Gillies, Donald C., Sandor L. Lehoczky, F. R. Szofran, Dale A. Watring, Helga A. Alexander and Gregory A. Jerman, J. Crystal Growth, 174, 101-107, 1997.
10. "Defect density characterization of detached-grown germanium crystals," Schweizer, M., S. D. Cobb, M. P. Volz, J. Szoke and F. R. Szofran, Defect density characterization of detached-grown germanium crystals," J. Crystal Growth, 235, 161-166 (2002).
11. "Comparison of Structure and Segregation in Alloys Directioanlly Solidified in Terrestrial and Microgravity Environments," Poirier, D. A., S. N. Tewari and J. C. Heinrich, Proceedings of the Microgravity Materials Science Conference, 471-476, 2000.
12. "Directional solidification microstructures in diffusive and convective regimes," Trivedi, R., H. Miyahara, P. Mazumder, E. Simsek and S. N. Tewari, J. Crystal Growth, 222, 365-379, 2001.
13. "Microstructure Effect on Dihedral Angle in Liquid-Phase Sintering," Liu, Jianxin and Randall M. German, Met. and Mat. Trans A, 32A, 165-169, 2001

14. "Coupled Growth in Hypermonotectics," Andrews, J. Barry, and Sam Coriell, Proceedings of the Microgravity Materials Science Conference, 45-51, 2000.
15. "Particle Engulfment and Pushing by Solidifying Interfaces: Part II. Microgravity Experiments and Theoretical Analysis," Stefanescu, D. M., F. R. Juretzko, B. K. Dhindaw, A. Catalina, S. Sen and P. A. Curreri, Met. and Mat. Trans A, 29A, 1697-1706, 1998.
16. Metals Handbook, Ninth Edition, Volume 2, Properties and Selection: Nonferrous Alloys and Pure Metals, p. 761, 1979.

**Photoelectric Effect**

Atom

Incident Photon

Photoelectron

$\mu_{PE} \sim K_1 Z^{4.5}/E^3$

(< 1 MeV) Total absorption of incident photon with the emission of a bound electron

**Compton Scatter**

Compton Electron

Atomic Electron

Incident Photon

Scattered Photon

$\mu_C \sim K_2 Z/f(E)$

(0.8-5MeV) Produces free electron and a scattered (less energetic) photon

**Pair Production**

Atomic Nucleus

Electron

Incident Photon

Positron

$\mu_{PP} \sim K_3 Z^2 g(E)$

(>3 MeV) Absorption of the incident photon with creation of an electron-positron pair

**Figure 1.   Photon Scattering Mechanisms**

243
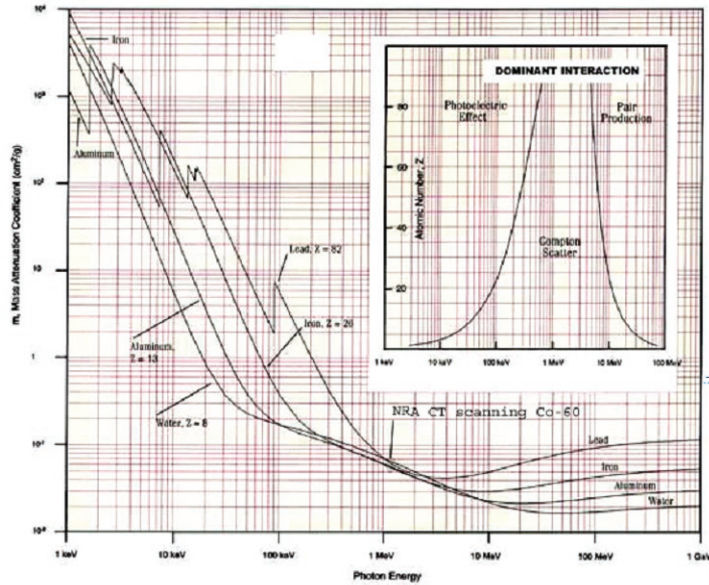
**Figure 2. Energy Dependence of Attenuation**



$I = I_0\, e^{-\int \mu(x,y)dl}$ **(Lambert's Law)**

$\int \mu(x,y)dl = -\ln(I/I_0)$ **(Ray-Sums)**

**The "ray-sums" are just the sum of all x-y attenuations along each ray path...**

$P(\Theta,\rho) = -\ln I(\Theta,\rho)/I_0$ (Radon's Theorem)

Basically, the $P(\Theta,\rho)$ are projections from which the $\mu(x,y)$ can be recovered:

$$\mu(x,y) = \int_0^{\pi}\int_{-\infty}^{\infty} P(\Theta,\rho)g(\rho-\eta)d\eta\,d\Theta$$

where: $g(r) = \pi^2/2\,(\delta(r)/r - 1/r^2)$  ($\delta$ the usual "delta" fnct.)

So, by any number of means, the $P(\Theta,\rho)$ recovered are the image data that produce the CT picture when mapped to a video screen. A popular method is via Fourier filtering a 2-D object space (2D FFT) transform to the 1D FFT image "picture."

**Figure 3. Fundamentals of the Radon Transformation**
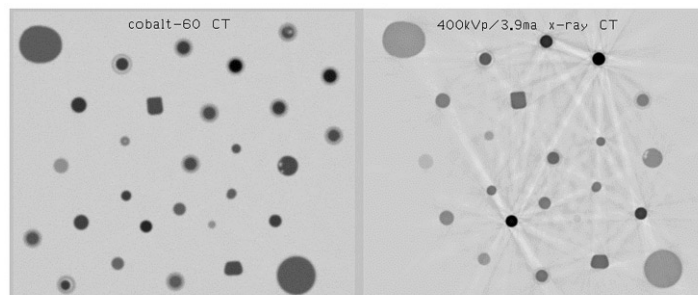


**Figure 4. CT scans of an array of standards with gamma(left) and X-Rays (right)**
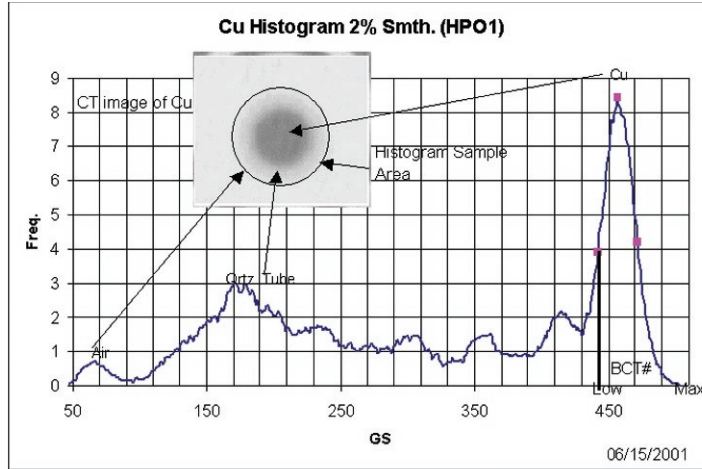
**Figure 5. Histogram of Cu standard within a fused silica tube**
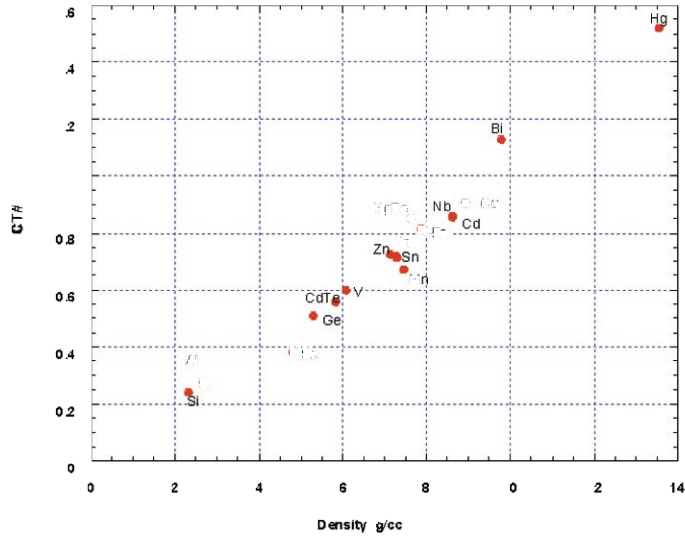


**Figure 6   Typical Standard Set for Quantitative Density Measurement**

245
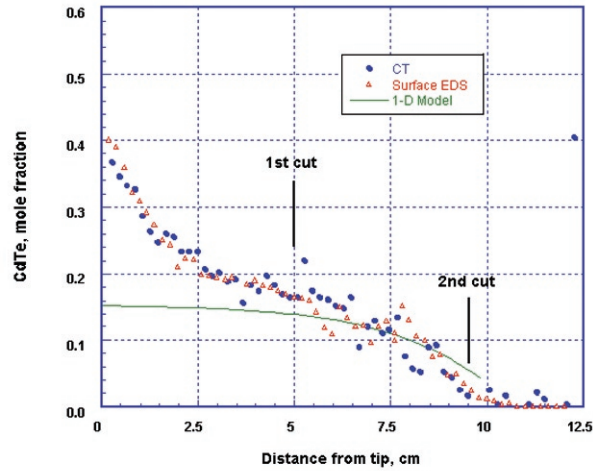
**Figure 7. CT determined composition data for a directionally solidified mercury cadmium telluride solid solution**
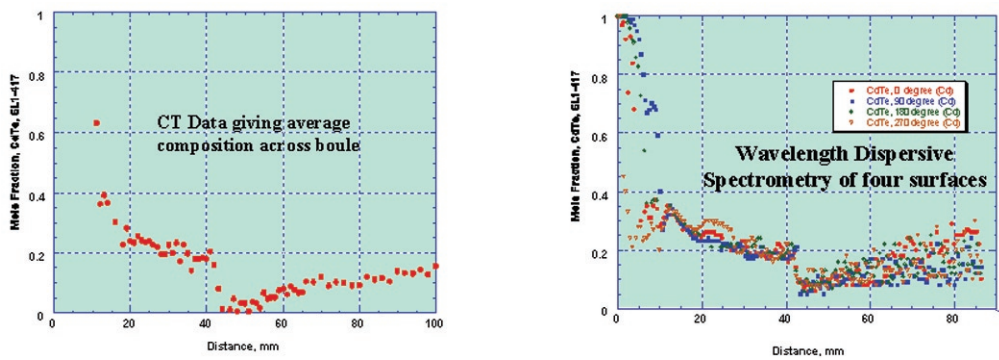


**Figure 8. A Comparison of CT (left) and Wavelength Dispersive Spectrometry (WDS) of four surfaces on a ground-grown crystal of HgCdTe**
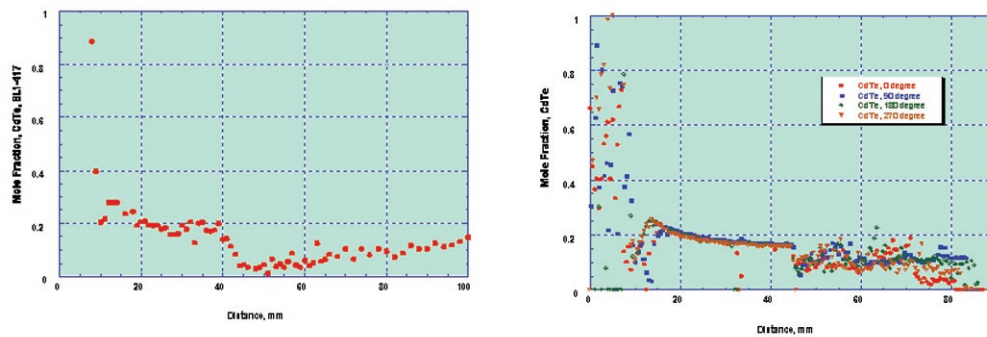


**Figure 9 . A Comparison of CT (left) and Wavelength Dispersive Spectrometry (WDS) of four surfaces on a microgravity-grown crystal of HgCdTe**

246

| Material | Alloy 1 | Alloy 2 | Δ Density | PI |
|---|---|---|---|---|
| PbSnTe | PbTe 8.27 g/cc | SnTe 6.53 g/cc | 26% | Fripp |
| HgCdTe | HgTe 8.112 | CdTe 5.852 | 38% | Lehoczky |
| GeSi | Ge 5.325 | Si 2.329 | 129% | Szofran |
| Pb-Sb | Pb 11.341 | Pb/.058Sb 11.071<br>Pb/.135Sb 10.74<br>Sb 6.697 | 2.4%<br>5.3%<br>40.9% | Poirier |
| Al-Cu | Al 2.699 | Al/.04Cu 2.948<br>Al/.33Cu 4.78<br>Al/.54Cu 7.06 | 9.2%<br>77%<br>162% | Trivedi |

**Table 1. Candidate Materials for Quantitative CT Scanning**
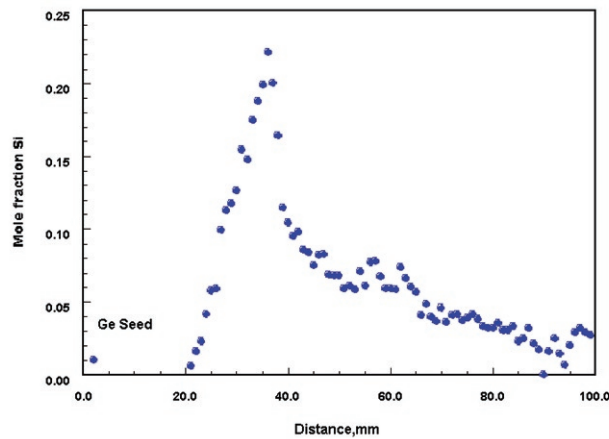


**Figure 10. CT of an alloy crystal of germanium-silicon seeded from germanium**



The data for density below (per the ASTM method) is from the average density of 32 CT slices at the elevations shown. Tue Mar 26 11:33:29 2002

Ge ref.

30.7mm 5.265gm/cc (0.0369std)

16.95mm 5.306gm/cc (0.0145std)

3.2mm 5.327gm/cc (0.0150std)

0mm

Ge-Si (Nom 2.5%Si)

Digital Radiograph

Results

Center 2.07 wt% Si or 5.2 atomic%

Bottom 0.67 wt% Si or 1.7 atomic%
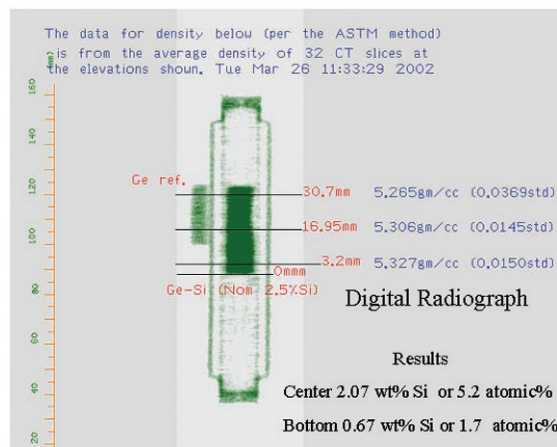
**Figure 11. Digital radiograph of a germanium-silicon alloy seed crystal**

247
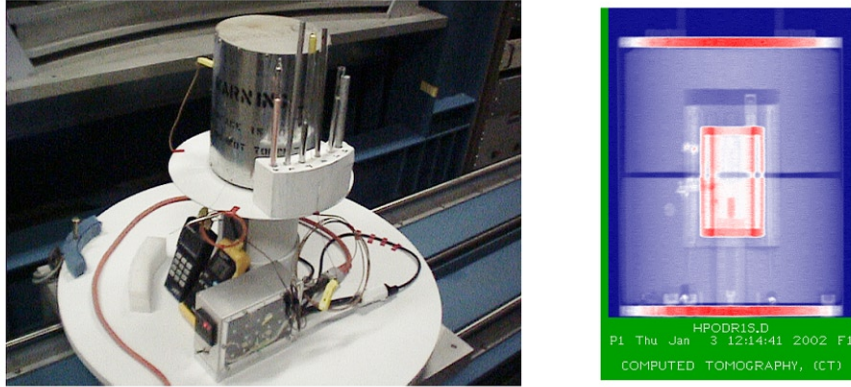
**Figure 12. MSFC-designed and built furnace residing on the CT translation stage at KSC (left), and digital radiograph of the furnace (right). Note the elemental standards outside the furnace**
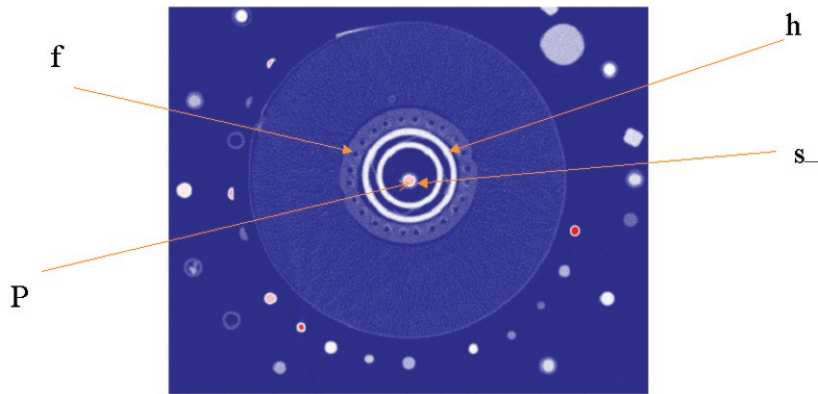


**Figure 13. CT section through furnace and lead sample (p). Furnace widings (f), heat pipe (h), and fused silica tube (s) all show clearly**

248
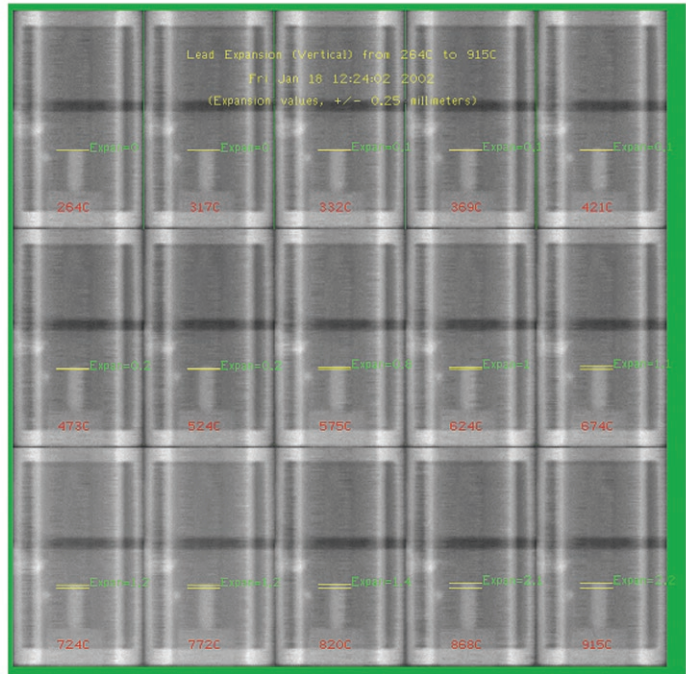
Figure 14. Digital Radiographs showing thermal expansion of Lead
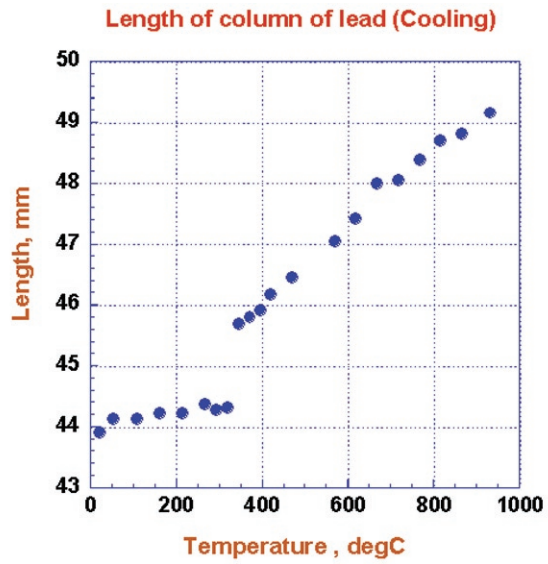


Figure 15. Dilation of lead on cooling from 900°C to room temperature
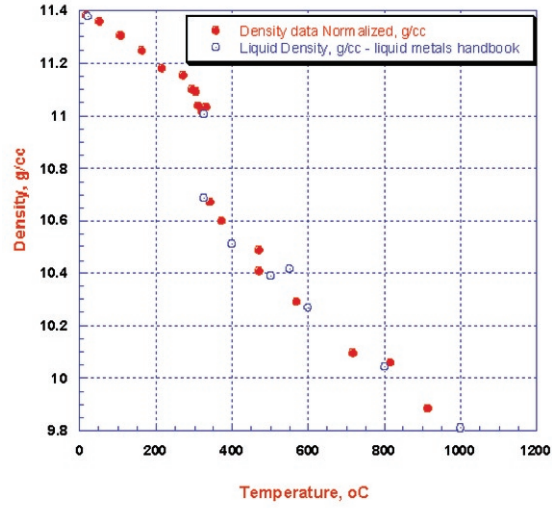
**Figure 16. Density of Lead as determined from CT Data**



a

b
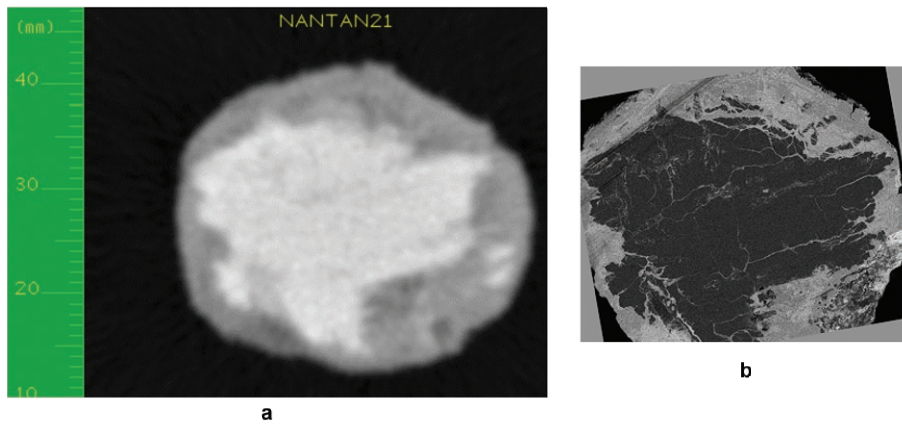
F gure 17  mage of  structure of Nantan meteorite from CT (left  and after cutting and polish ng (right).  The polished surface shows an oxygen image determined using electron microprobe (light color means higher concentration)

250

a



b

Figure 18. The Mundrabilla meteorite. 6 ton piece as found (upper), and part of the 80 cm slab as polished at MSFC (lower). Note the fanshaped graphite (outlined)



Figure 19  Macrophotograph of the structure of the Mundrab  a meteorite.  The  ron-nickel Widmanstatten structure  s demonstrated by the grain on the bottom right, while the striated sulfide structure  s the troilite with paral el daubreelite inclusions.
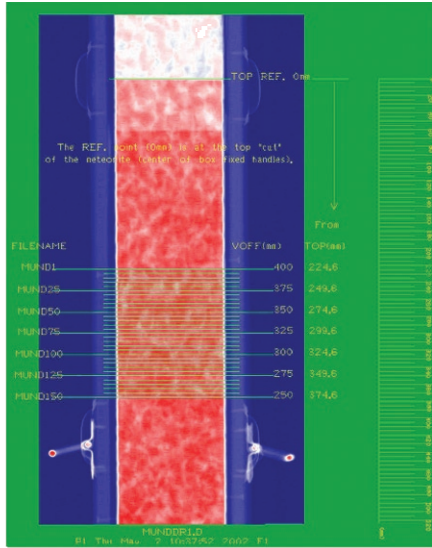
Figure 20. A Digital Radiograph of the Mundrabi a meteorite demonstrating the region subjected to the first series of CT scans.
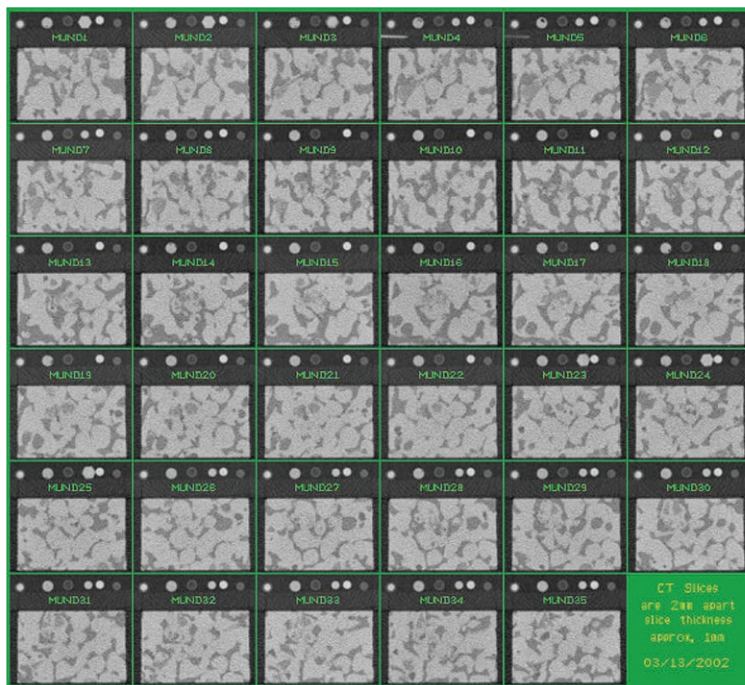


Figure 21. Thirty six of the first 150 CT scans made on the Mundrabi a meteorite

252

FeS (Cr)

FeNi
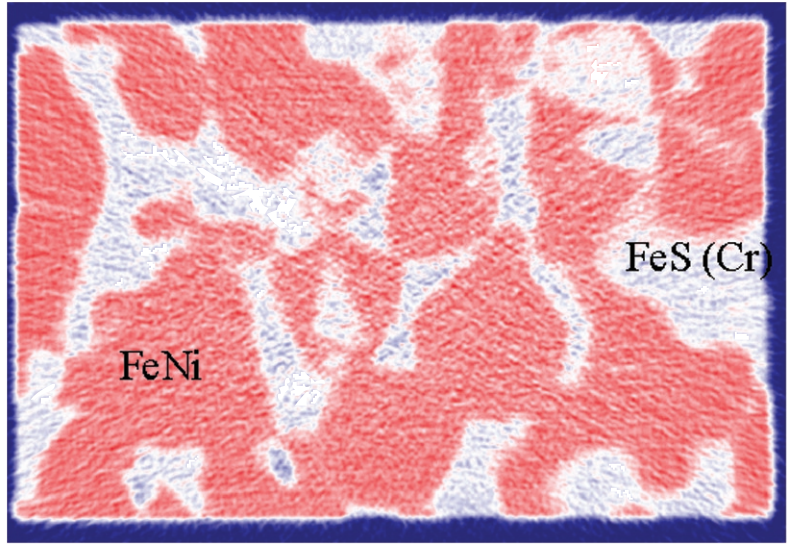
**Figure 22.  A color enhanced CT scan show ng the metall c phase (dark  red) and the  sulfide phase ( ight, blue)**